



## Molecular engineering of microporous crystals: (IV) Crystallization process of microporous aluminophosphate $\text{AlPO}_4\text{-11}$

Tao Cheng<sup>b,1</sup>, Jun Xu<sup>c,1</sup>, Xu Li<sup>a</sup>, Yi Li<sup>a</sup>, Bin Zhang<sup>a</sup>, Wenfu Yan<sup>a,\*</sup>, Jihong Yu<sup>a</sup>, Huai Sun<sup>b</sup>, Feng Deng<sup>c</sup>, Ruren Xu<sup>a,\*</sup>

<sup>a</sup> State Key Laboratory of Inorganic Synthesis and Preparative Chemistry, College of Chemistry, Jilin University, 2699 Qianjin Street, Changchun 130012, PR China

<sup>b</sup> College of Chemistry and Chemical Engineering, Shanghai Jiaotong University, Shanghai 200240, PR China

<sup>c</sup> Wuhan Center for Magnetic Resonance, State Key Laboratory of Magnetic Resonance and Atomic and Molecular Physics, Wuhan Institute of Physics and Mathematics, The Chinese Academy of Sciences, Wuhan 430071, PR China

### ARTICLE INFO

#### Article history:

Received 7 October 2011

Received in revised form 14 November 2011

Accepted 16 November 2011

Available online 30 November 2011

#### Keywords:

Aluminophosphate

$\text{AlPO}_4\text{-11}$

Fragment

Crystallization

Zeolite

### ABSTRACT

The products of microporous aluminophosphate  $\text{AlPO}_4\text{-11}$  crystallized for different periods of time were freeze-dried and characterized by XRD and NMR techniques. Six crystallographically distinct Al- and P-centered large fragments and 34 small fragments of dimer (Al–P), trimer (Al–P–Al and P–Al–P), tetramer (Al–P<sub>3</sub> and P–Al<sub>3</sub>), pentamer (Al–P<sub>4</sub> and P–Al<sub>4</sub>), and 4- and 6-membered rings were extracted from the framework of  $\text{AlPO}_4\text{-11}$ . Each of the six large fragments contained two completed coordination layers surrounding the centered atom. The shielding tensors of the Al and P atoms of the fragments were calculated using the quantum mechanics density functional theory. The experimentally observed chemical shifts of Al or P from the well-crystallized  $\text{AlPO}_4\text{-11}$  were assigned to the shielding tensors of the center atoms of the six large fragments and were further used as references in the determination of the chemical shifts of the Al or P atoms in the small fragments. A comparison of the calculated chemical shifts of the Al and P atoms in the small fragments to the experimental data of the products isolated at different crystallization periods suggested that the fragments of dimers, trimers of the form Al–P–Al, tetramers of the form P–Al<sub>3</sub>, and pentamers may exist in the crystallization process of  $\text{AlPO}_4\text{-11}$ . On the basis of these observations regarding the putative small fragments, a possible crystallization process of  $\text{AlPO}_4\text{-11}$  was proposed.

© 2011 Elsevier Inc. All rights reserved.

### 1. Introduction

Zeolites and related microporous crystalline materials, which have periodic three-dimensional frameworks and well-defined pore structures, have attracted much interest due to their wide applications in catalysis, ion-exchange, separation, and adsorption [1–6]. Although numerous zeolitic structures have been successfully synthesized by using methods based on empirical findings or by exploring synthetic parameters through trial and error [7], it is of importance to rationally design and synthesize additional zeolitic structures with desired architectures and properties. This rational design requires a clear understanding of the reaction mechanism and crystallization process involved in zeolite synthesis. The previous study of the crystallization process is based on the crystal nucleation and growth theory [8–10]. This theory dictates that the formation of a crystalline entity from a solution starts through a nucleation process, and the increase in size is achieved

by a growth process. Nucleation is usually defined as a series of atomic or molecular processes by which the atoms or molecules rearrange into a cluster of the product phase that is large enough to have the ability to grow irreversibly to a macroscopically larger size. The cluster is called a nucleus or critical nuclei. The crystal growth is a series of processes by which an atom, a molecule, or a fragment is incorporated into the surface of a nucleus, causing an increase in size. However, the structure of the nucleus has never been clearly described thus far, and the nuclei have never been separated during the synthesis of zeolites and related microporous crystalline materials.

The two main mechanisms appeared in the study of the reaction mechanism and crystallization process are the following: the solution-mediated transport mechanism and the solid hydrogel transformation mechanism [11–13]. The solution-mediated transport mechanism states that the crystallization process involves the dissolution of the hydrogel followed by the transport of the small fragments to the nucleation sites where the crystal growth takes place. However, the solid hydrogel transformation mechanism claims that the crystallization process involves the reorganization of the solid phase from an initially amorphous state to one with

\* Corresponding authors. Fax: +86 431 85168609 (R. Xu).

E-mail addresses: [yanw@jlu.edu.cn](mailto:yanw@jlu.edu.cn) (W. Yan), [rrxu@jlu.edu.cn](mailto:rrxu@jlu.edu.cn) (R. Xu).

<sup>1</sup> These authors contributed equally to this work.

long-range ordering. In 2005, Cundy et al. summarized the previous studies on the reaction mechanism and crystallization process of zeolites in a comprehensive review [14]. In that review, the authors pointed out that the arguments about whether key events occur in the solid phase or in solution are sterile and unnecessary. At the end of the survey, Cundy et al. proposed a generalized mechanism for zeolite synthesis, which is based primarily on the solution-mediated transport mechanism.

In addition to the arguments on the solution- or solid-related reaction mechanisms, the studies of the reaction mechanism also focused on the investigation of the early stage of the crystallization process [15–38]. For example, Burkett et al. studied a D<sub>2</sub>O-containing synthesis gel that produced pure-silica ZSM-5 with an NMR technique and found that the close contact between the protons of tetrapropylammonium (TPA) ions of the organic structure-directing agent and the silicon atoms of the inorganic moiety had been established before the long-range order of the crystalline pure silica ZSM-5 structure is formed [15,16]. Later, by combining the *in situ* wide-angle, small-angle, and ultra-small-angle X-ray scattering techniques, de Moor et al. studied the crystallization process of pure silica ZSM-5 templated by tetrapropylammonium ions [17]. On the basis of the collected data, de Moor et al. concluded that the key primary building unit composed of TPA and silicate is approximately 2.8 nm in size. The primary building units aggregated together to form entities up to 10 nm in size. These entities were called nuclei, which initiated the growth of pure silica ZSM-5. However, the exact structure of the primary building units and the larger entities was not described. A similar idea has also been developed by Martens and co-workers at Leuven [18–22]. By using a wide variety of experimental techniques, Martens and co-workers studied in detail the crystallization process of pure silica ZSM-5 templated by tetrapropylammonium ions. They identified slab-shaped particles (denoted as “nanoslabs”) with dimensions of  $1.3 \times 4.0 \times 4.0$  nm. The nanoslabs have the ZSM-5 structure with nine intersections per particle. Each of these intersections contains a TPA cation. The aggregation of such nanoslabs results in larger particles and, ultimately, in the crystalline product. However, there is no detailed information about how these nanoslabs formed, and this observation is questioned as well [23–25]. In contrast to the above studies, which were conducted under hydrothermal conditions, Tsapatsis and co-workers studied the crystallization process of pure silica ZSM-5 templated by tetrapropylammonium hydroxide (TPAOH) at room temperature [26–28]. They monitored the evolution of nanoparticles that formed spontaneously upon the hydrolysis of tetraethylorthosilicate in aqueous solutions of TPAOH at room temperature for more than one year up to and beyond pure silica ZSM-5 crystal formation. On the basis of their data, Tsapatsis and co-workers proposed that the crystalline pure silica ZSM-5 evolved from approximately 5-nm precursor nanoparticles through oriented attachment and that the nanoparticles actively participate in the nucleation and crystallization processes. However, the key step, i.e., the establishment of long-range order in the precursor nanoparticles, was not illustrated. Therefore, the detailed and exact structural information for the species formed in the early stage of the crystallization process is critical to understanding the reaction mechanism and crystallization process.

Recently, we developed a strategy for investigating the crystallization processes of microporous crystalline compounds and a method based on mathematical matrix and graph theories to describe the open framework of microporous crystals and the fragments that may be formed in the early stages of the crystallization process [39,40]. When the crystallization process starts, the complicated condensation reaction between Al and P sources under the conditions at the time will occur, forming the hydrogel with specific chemical composition and structure and the liquid phase located in

the void of the hydrogel. Small fragments (species) of aluminophosphate with specific structure and configuration can be found in the liquid phase. Along with the crystallization process, the small fragments are assembled around the structure-directing agent. With our strategy, exact structural information for each species that formed during the period of crystallization or for a core unit from which a single crystal was grown could be obtained. The solid phase isolated at different crystallization periods can be characterized by various techniques. By comparing the simulated characterization information of these species with the experimental characterization data, it is possible to identify the fragments formed during the crystallization process. On the basis of these observations regarding the putative small fragments, we can further investigate and discuss the specific details of a possible crystallization process.

In this study, we investigated the crystallization process of AlPO<sub>4</sub>-11. A method was developed to distinguish the possible and unlikely fragments formed in the crystallization process. The present study represents a step forward in understanding the crystallization of microporous aluminophosphates at the molecular level.

## 2. Experimental section

### 2.1. Synthesis

A typical procedure for the preparation of a reaction mixture is as follows: 1.94 mL of 85% phosphoric acid was stirred with 2.0 g of water, and 2.0 g of boehmite was added. The mixture was stirred well for approximately 10 min, and then 2.45 mL of di-(*i*-propyl)amine (D-IPA) was added dropwise with continuous stirring. The gel was further stirred for approximately 20 min at ambient temperature to ensure homogeneity. The reaction mixture with a molar ratio of Al<sub>2</sub>O<sub>3</sub>:P<sub>2</sub>O<sub>5</sub>:1.2 D-IPA:15 H<sub>2</sub>O was loaded into a Teflon-lined autoclave (volume: 20 mL). The autoclaves containing approximately equal amounts of the reaction mixture were then placed in an oven pre-heated to 180 °C. The timing started when all of the autoclaves were loaded into the oven. The autoclaves were heated for different periods of time and quenched in cold water. The product from each autoclave was divided into two parts. One-half of the product was freeze-dried (–60 °C), which ensured the complete collection of all small species formed during the crystallization process. The liquid and solid phase of the other half of the product was separated by centrifugation (9500 rpm or 8475g), and the solid phase to be used as a reference was dried at room temperature. The dried samples were sealed well for later characterization.

The powder XRD patterns were recorded on a Rigaku diffractometer equipped with a graphite monochromator using Cu K $\alpha$  radiation ( $\lambda = 1.5418$  Å) at 50 kV and 200 mA. The scanning angle ( $2\theta$ , where  $\theta$  is the Bragg angle) used ranged from 4° to 40° in steps of 0.02°, and the sampling interval was 0.1 s. TG analysis with a heating rate of 10 °C/min was performed in air using a TGA Q500 analyzer from TA Instruments in high-resolution mode.

### 2.2. NMR characterization

All NMR experiments were performed on a Varian Infinity-plus 400 spectrometer operating at a magnetic field strength of 9.4 T. The resonance frequencies at this field strength were 161.9 and 104.2 MHz for <sup>31</sup>P and <sup>27</sup>Al, respectively. A chemagnetics 5-mm triple-resonance MAS probe with a spinning rate of 8 kHz was employed to acquire <sup>31</sup>P and <sup>27</sup>Al NMR spectra. The <sup>27</sup>Al MAS spectra were acquired using a single pulse sequence with a short radio frequency (rf) pulse of 0.5 s (corresponding to a  $\pi/15$  flip angle) and a pulse delay of 1.0 s. The pulse length for <sup>27</sup>Al was

measured on a 1 M  $\text{Al}(\text{NO}_3)_3$  solution. Single-pulse  $^{31}\text{P}$  MAS NMR experiments with  $^1\text{H}$  decoupling were performed with a  $90^\circ$  pulse width of 4.6 s, a 180 s recycle delay, and a  $^1\text{H}$  decoupling strength of 42 kHz. The chemical shifts were referenced to a 85%  $\text{H}_3\text{PO}_4$  solution for  $^{31}\text{P}$  and a 1 M  $\text{Al}(\text{NO}_3)_3$  solution for  $^{27}\text{Al}$ .

### 2.3. Simulation

The non-bonding interaction between the inorganic host and the guest species was modeled using the consistent valence force field (CVFF) [41]. Periodic boundary conditions (PBCs) were applied. The electrostatic terms were calculated using the Ewald summation. The atomic charges for the D-iPA cations and  $\text{OH}^-$  anions were calculated by density functional theory (DFT) studies at B3LYP/6-31G (d,p) levels using the GAUSSIAN 03 W program [42,43]. The net charges for the O, Al, and P atoms in the framework were fixed to  $-1.2$ ,  $1.4$ , and  $3.4$ , respectively. The framework structure of the  $\text{AlPO}_4$ -11 was obtained from the literature [44] and fixed for all of the subsequent calculations. Simulated annealing calculations were performed using Materials Studio to find the best configuration and location of the guest species [45]. Two D-iPA cations, one water molecule and two hydroxyl ions were manually inserted into one unit cell of  $\text{AlPO}_4$ -11. Considering all possible combinations, 24 different starting configurations were obtained. To find the configuration with the lowest energy, simulated annealing calculations were performed on these 24 models. One hundred annealing cycles were carried out for each model. In each annealing cycle, the structure model was heated from 300 K to 900 K in temperature increments of 12 K (50 ramps) and cooled down in the same way. Five hundred NVT steps of 1.0 fs were run in each heating step. The geometry of the structural model was optimized at the end of each annealing cycle; thus, we had  $24 \times 100$  structural models. Among the  $24 \times 100$  structural models we obtained from simulated annealing, only 10 were actually unique. The structural model of the lowest energy contained one D-iPA cation in each 10-ring channel; one water molecule and two hydroxyl ions were in different 6-ring channels. The structural model with the lowest potential energy was chosen for further analysis (Fig. 1).

The calculations of the shielding tensors of the Al and P atoms in the fragments were performed using the quantum mechanics den-

sity functional theory (DFT) [46]. The B3LYP functional and the 6-31 g (d, p) basis set were used in the DFT calculations. The dangling bonds in the constructed molecular fragments were saturated by adding hydrogen atoms so that the calculated molecules were in closed-shell electronic configurations. The shielding tensors were calculated using the gauge-independent atomic orbital method (GIAO) [47]. The DFT calculations were performed using the GAUSSIAN 03 W program [43].

## 3. Results and discussion

### 3.1. X-ray diffraction study of the crystallization process of $\text{AlPO}_4$ -11

$\text{AlPO}_4$ -11 is a member of microporous crystalline aluminophosphates reported by Wilson et al. in 1982 [48–53]. The structure of the calcined  $\text{AlPO}_4$ -11, solved by a Rietveld refinement of neutron time-of-flight data [44], is built of alternating  $\text{AlO}_4$  and  $\text{PO}_4$  tetrahedra linked via oxygen atoms. The open framework of  $\text{AlPO}_4$ -11 as shown in Fig. 1 comprises three distinct tetrahedral crystallographic sites each for aluminum (labeled as Al1, Al2, and Al3, respectively) and phosphorus (labeled as P4, P5, and P6, respectively). The crystallization process of  $\text{AlPO}_4$ -11 has been monitored using *in situ* or *ex situ* characterization techniques by Huang and by our group [54–56]. In Huang's work, a number of intense peaks in the product's XRD pattern that did not belong to  $\text{AlPO}_4$ -11 were observed [54,55]. Interestingly, these peaks did not appear in the XRD patterns of water-rinsed samples. Therefore, the authors attributed those intense peaks to a highly soluble, layered, semi-crystalline aluminophosphate intermediate with a three-dimensional structure that bore some similarity to the structure of  $\text{AlPO}_4$ -11. In our study, we observed a significant influence of the water content of the synthesis mixture on the crystallization process of  $\text{AlPO}_4$ -11 [56]. Under high water content conditions ( $\text{Al}_2\text{O}_3:\text{H}_2\text{O} = 1:20\text{--}69$ ), an  $\text{AlPO}_4$ -5 intermediate formed first, and it later co-existed with  $\text{AlPO}_4$ -11. In the last stage of crystallization, the crystalline  $\text{AlPO}_4$ -5 completely disappeared, and well-crystallized  $\text{AlPO}_4$ -11 was obtained. Under low water content conditions ( $\text{Al}_2\text{O}_3:\text{H}_2\text{O} = 1:15$ ), the  $\text{AlPO}_4$ -11 was directly crystallized from the initial mixture. In the latter study, all of the solid samples were washed with deionized water. In the present study, the ratio of  $\text{Al}_2\text{O}_3$  to  $\text{H}_2\text{O}$  was set as 1:15, corresponding to the low water condition in our previous study [56]. The product was freeze-dried, which ensured the complete collection of all small species formed during the crystallization process.

Fig. 2 shows the simulated XRD pattern of  $\text{AlPO}_4$ -11 and the experimental patterns of the samples isolated throughout the

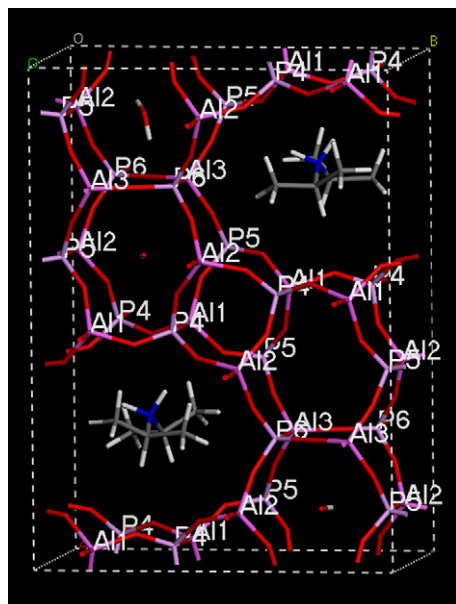


Fig. 1. The framework structure of  $\text{AlPO}_4$ -11.

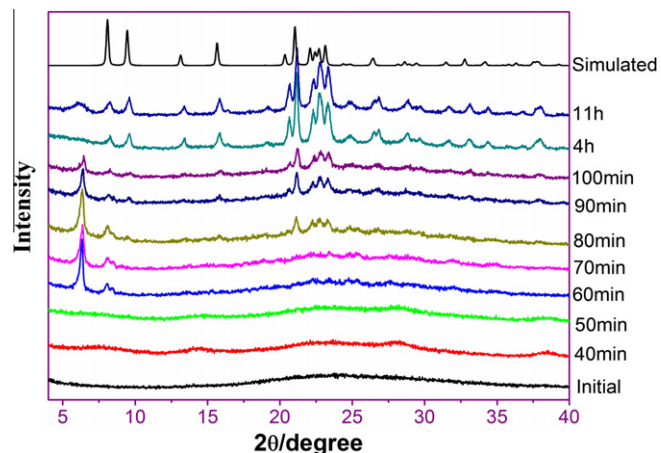
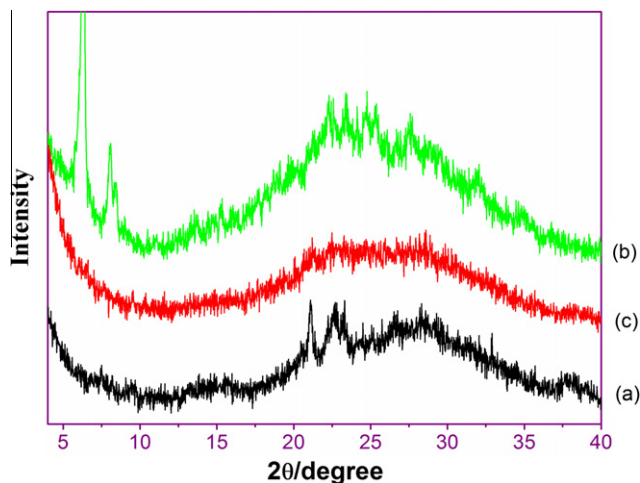


Fig. 2. The simulated XRD pattern of  $\text{AlPO}_4$ -11 and the experimental patterns of the samples isolated throughout the hydrothermal treatment period.

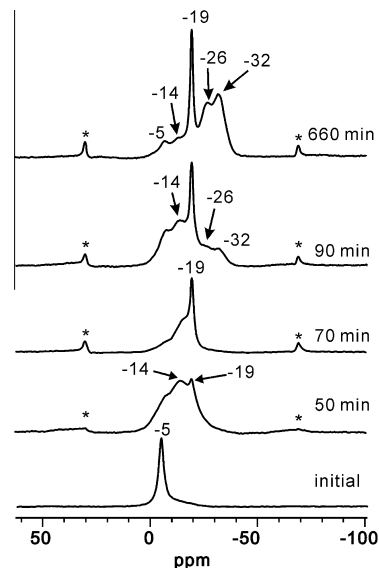


**Fig. 3.** The XRD patterns of the 60 min samples treated by (a) centrifugation or (b) freeze-drying and the corresponding washed sample (c).

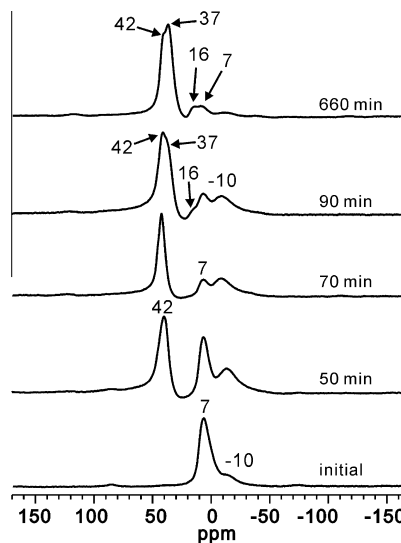
hydrothermal treatment period. In the initial mixture and the products heated for 40 or 50 min, no long-range order phase of aluminophosphate was observed. When the heating time was prolonged to 60 min, a number of intense peaks at the low-angle region of 2 appeared. However, these intense peaks completely disappeared when the second sample from the same autoclave was separated by centrifugation [56], indicating that the long-range order phase is highly soluble in water. To determine whether this speculation is correct, this freeze-dried 60-min sample was quickly rinsed again with water at room temperature. The corresponding experimental XRD patterns are shown in Fig. 3. It is clear that the long-range order phase generating the intense reflections at the low-angle region of 2 is completely dissolved in water. According to previous studies of the synthesis of  $\text{AlPO}_4\text{-11}$  and other aluminophosphates with open frameworks under hydro/solvothermal conditions, this highly soluble long-range order phase is probably a di-(*i*-propyl)ammonium phosphate [57–63]. When the heating time was prolonged to 70 min or longer, typical diffraction peaks of  $\text{AlPO}_4\text{-11}$  at the low- and mid-angle ranges of 2 emerged, and the intensity of the diffraction peaks belonging to di-(*i*-propyl)ammonium phosphate gradually decreased. These latter peaks completely disappeared when the highly crystalline  $\text{AlPO}_4\text{-11}$  was obtained.

### 3.2. NMR study of the crystallization process of $\text{AlPO}_4\text{-11}$

To obtain detailed local structural information about the species formed during the crystallization process, we characterized the samples with an NMR technique. The  $^{31}\text{P}$  and  $^{27}\text{Al}$  MAS NMR spectra of the samples are shown in Figs. 4 and 5, respectively. In Fig. 4, a sharp signal at  $-5$  ppm and a broad upfield signal at  $-10$  to  $-30$  ppm with significantly low intensity are observed in the initial mixture. The sharp signal can be assigned to the possible di-(*i*-propyl)ammonium phosphates dissolved in the solution, whereas the broad signal is assigned to amorphous aluminophosphate containing Al–O–P linkages. After heating the initial mixture for approximately 50 min, the broad signal grows, and distinct signals at  $-14$  and  $-19$  ppm can be resolved. The former signal can be assigned to the P atom in the amorphous aluminophosphate phase, whereas the latter signal can be assigned to the P site with a high coordination number around the Al atom. As observed above, the signal at  $-19$  ppm is present in the well-crystallized  $\text{AlPO}_4\text{-11}$ , suggesting that the environment of this P site is same or very similar to that of a P site in the well-crystallized  $\text{AlPO}_4\text{-11}$ . The absence of this signal in the corresponding centrifugation-separated sample



**Fig. 4.** The  $^{31}\text{P}$  MAS NMR spectra of the initial mixture and the samples isolated throughout the hydrothermal treatment period. Asterisks indicate spinning sidebands.



**Fig. 5.** The  $^{27}\text{Al}$  MAS NMR spectra of the initial mixture and the samples isolated throughout the hydrothermal treatment period.

suggests that the fragments containing this P site are extremely small and remain in the liquid phase during the centrifugation separation [56]. By prolonging the heating time to 70 min, the intensity of the signal at  $-19$  ppm is significantly enhanced, which compressed the  $-5$  ppm signal corresponding to the di-(*i*-propyl)ammonium phosphates that existed in the form of long-range order. When the heating time is further increased to 90 min, well-resolved XRD peaks of  $\text{AlPO}_4\text{-11}$  are observed (Fig. 2), and two new signals at  $-26$  and  $-32$  ppm are observed (Fig. 4). These two new signals can be assigned to the P sites in the structure of  $\text{AlPO}_4\text{-11}$ . Interestingly, the strong signal at  $-19$  ppm observed in the samples heated for 90 min or 11 h is not clearly distinguished in the corresponding centrifugation-separated samples [56]. In addition, the intensity of this signal in the 11 h sample is unreasonably high, suggesting that this strong signal is not only from the structure of  $\text{AlPO}_4\text{-11}$  but also from the extremely small fragments that are collected in the solid form during the freeze-drying treatment. These



small species remain in the liquid phase and are not included in the solid phase in the centrifugation separation method. After subjection to the freeze-drying treatment, the small species are all collected in the solid form. A small amount of unconsumed amorphous aluminophosphates (–14 ppm) and di-(*i*-propyl)ammonium phosphates (–5 ppm) are also observed in the spectrum of the 11 h sample.

Fig. 5 shows the  $^{27}\text{Al}$  MAS NMR spectra of the initial mixture and the samples isolated throughout the hydrothermal treatment period. In the initial mixture, the octahedral Al (–10 ppm) is more apparent than that in the corresponding centrifugation-separated sample [56]. The 50 min spectrum is similar to that of the corresponding centrifugation-separated sample, but it differs in the relative intensity of the three signals [56]. A large amount of four-coordinate Al species (42 ppm) were formed. Upon heating for 90 min, a shoulder signal at 37 ppm was resolved in addition to the five-coordinate Al (16 ppm) that was observed. By combining the XRD results shown in Fig. 2, it can be concluded that the Al atom corresponding to the shoulder signal at 37 ppm is associated with the framework of  $\text{AlPO}_4\text{-11}$ , whereas the signal at 42 ppm is from the species remaining in the liquid phase. After the crystallization is completed (11 h), the tetrahedral Al sites in the crystallized framework that give rise to the signals at 42 and 37 ppm dominate the spectrum.

### 3.3. Location of guest species in the channels via simulation

The structure of the calcined  $\text{AlPO}_4\text{-11}$  was solved by a Rietveld refinement of neutron time-of-flight data, and the framework has been proved to be neutral. Therefore, the exact information on the number and position of guest species in the channel of as-synthesized  $\text{AlPO}_4\text{-11}$  is not available thus far. In the original literature describing  $\text{AlPO}_4\text{-11}$ , approximately two di-(*n*-propyl)amine molecules and one-half of a water molecule in one unit cell were suggested [49]. Later, Tapp et al. systematically studied the influence of the electronic and steric effects of the structure-directing agent on the formation of  $\text{AlPO}_4\text{-11}$  [57]. The results of their studies suggested that the match in size between the structure-directing agent and the unit cell *c*-dimension (i.e., approximately 8.4 Å) is critical for the successful formation of  $\text{AlPO}_4\text{-11}$  and that each channel in one unit cell contained one di-(*i*-propyl)amine molecule (i.e., two di-(*i*-propyl)amine molecules per unit cell). However, in a recent study, it was claimed that each unit cell of  $\text{AlPO}_4\text{-11}$  contained 3.1 protonated di-(*n*-propyl)amine molecules (balanced with a  $\text{OH}^-$  anion) and 3.4 water molecules on average [64].

The state of the organic structure-directing agent in the channel of  $\text{AlPO}_4\text{-11}$  was also studied by Dufau et al. [65] and Han et al. [64]. Dufau et al. studied the template evaporation from the channel of  $\text{AlPO}_4\text{-11}$  using a sample controlled thermal analysis (SCTA) and concluded that the di-(*n*-propyl)amine was hydrated in the form of  $(\text{C}_3\text{H}_7)_2\text{NH}_2^+\text{OH}^-$ . Using a Raman characterization technique, Han et al. confirmed that the di-(*n*-propyl)amine that was trapped within the channel of  $\text{AlPO}_4\text{-11}$  was present in the protonated form. In addition, the  $^{13}\text{C}$  MAS NMR spectra of the initial mixture and the samples isolated throughout the hydrothermal treatment period and the *in situ* Raman experiments in our previous study suggested that the di-(*i*-propyl)amine molecules were protonated [56]. Therefore, we assume that the di-(*i*-propyl)amine is present as  $(\text{C}_3\text{H}_7)_2\text{NH}_2^+\text{OH}^-$  in the channel of  $\text{AlPO}_4\text{-11}$ .

A thermogravimetric analysis performed in high-resolution mode shows two steps of weight loss from ambient temperature to 800 °C (Fig. 6). The weight loss of approximately 1 wt.% for the first step from ambient temperature to 140 °C is attributed to the physically adsorbed water. The weight loss of approximately 9 wt.% for the second step from 140 to 800 °C is attributed to the decomposition of  $(\text{C}_3\text{H}_7)_2\text{NH}_2^+\text{OH}^-$  and suggests that each unit cell

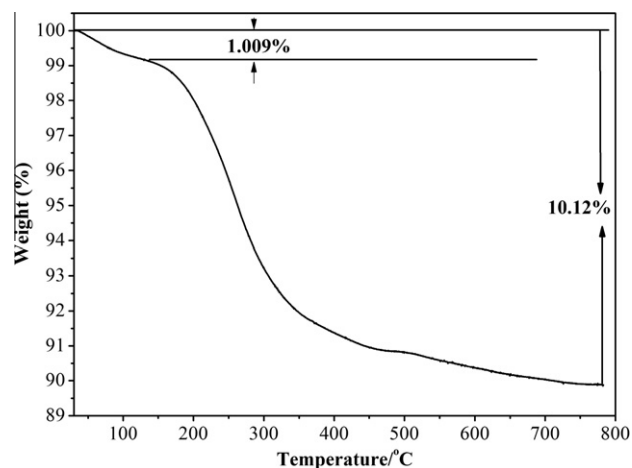


Fig. 6. The thermogravimetric (TG) analysis curve of as-synthesized  $\text{AlPO}_4\text{-11}$ .

Table 1

The experimental chemical shifts of Al and P in the framework of  $\text{AlPO}_4\text{-11}$ .

Elements	Al	P		
Chemical shifts (ppm)	37	–19	–26	–32

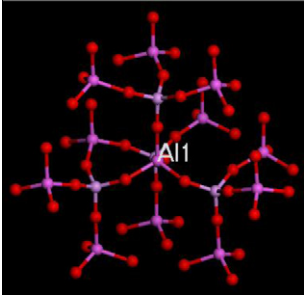
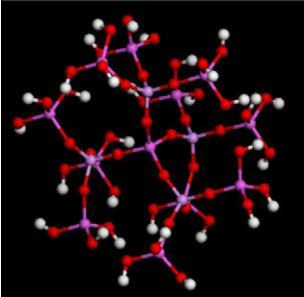
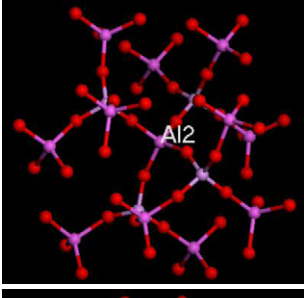
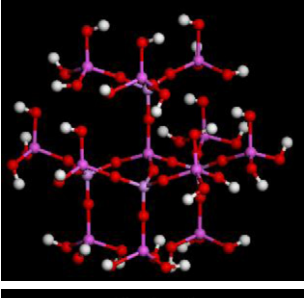
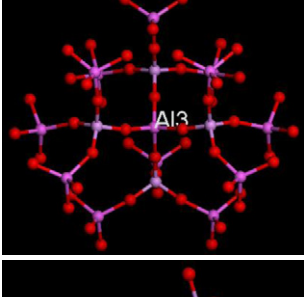
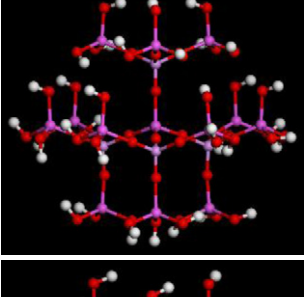
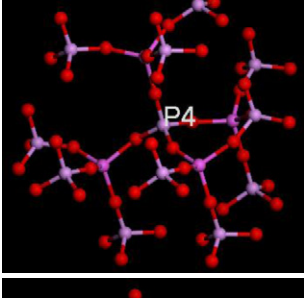
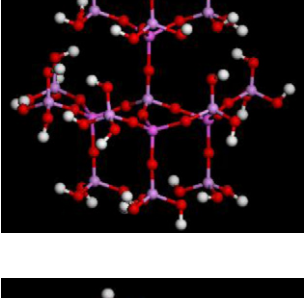
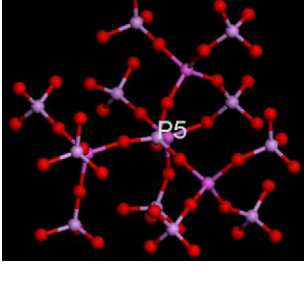
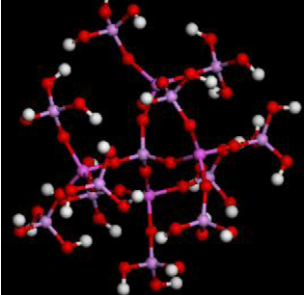
of  $\text{AlPO}_4\text{-11}$  contains approximately two  $(\text{C}_3\text{H}_7)_2\text{NH}_2^+\text{OH}^-$  molecules. Therefore, we assume that each unit cell of  $\text{AlPO}_4\text{-11}$  contains two  $(\text{C}_3\text{H}_7)_2\text{NH}_2^+\text{OH}^-$  molecules and one water molecule. Subsequently, the positions of these two organic species were determined by a simulation based on density functional theory and molecular dynamics. The location of the guest species and the structure of the  $\text{AlPO}_4\text{-11}$  viewed along the [001] direction are shown in Fig. 1. The T atom of the framework that is closest to the N atom of di-(*n*-propyl)amine is P4, suggesting that the protonated di-(*n*-propyl)amine has the strongest interaction with the species or fragment containing this P atom at the beginning of crystallization. Thus, the composite (or core unit, according to Ref. [39]) containing the protonated di-(*n*-propyl)amine and the fragment with this P atom might be the onset of the crystallization.

### 3.4. Extraction of the fragments from the framework of $\text{AlPO}_4\text{-11}$

According to our understanding of the crystallization process of a microporous crystal, the crystallization process can be described as a successive self-assembly process of small fragments. During the crystallization process, the source materials in the form of isolated molecules react with each other to form inorganic fragments. These inorganic fragments are assembled together around the structure-directing agent to form specific composites, which are finally included into the final structure. The inorganic fragments can capture another structure-directing agent to complete the growth process. In fact, the inorganic fragments of trimer, tetramer, and pentamer have been recognized in the studies on the amorphous phases formed during the synthesis of microporous material  $\text{AlPO}_4\text{-5}$  [66]. Considering the fact that the bond length and angle are difficult to change when a closed shape such as ring or double ring is formed, we speculate that the structural information of the fragments that are formed during the crystallization process may be the same or very similar to those in the final structure. Therefore, extracting some fragments from the final structure to provide information about the starting point of the species formed during the crystallization process is reasonable. Guided by this speculation, we extracted some fragments from the structure of

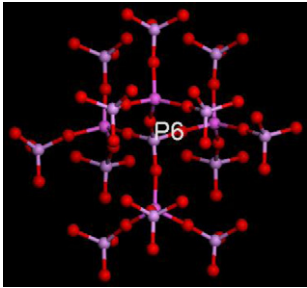
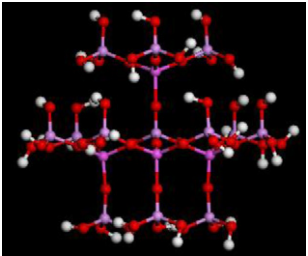
**Table 2**

The structures and formulas of the six large fragments before and after the calculation and the calculated shielding tensors and related chemical shifts.

Center atom	Image-before calculation	Formula-before calculation	Image-after calculation	Formula-after calculation	Shielding tensors	Chemical shifts (ppm)
Al1		$\text{Al}_{12}\text{P}_4\text{O}_{48}^{40-}$		$\text{Al}_{12}\text{P}_4\text{O}_{48}\text{H}_{32}^{8-}$	Al:562.7 P:414.0 P:414.7 P:414.6 P:414.6	Al:36 P:–20 P:–21 P:–21 P:–21
Al2		$\text{Al}_{12}\text{P}_4\text{O}_{48}^{40-}$		$\text{Al}_{12}\text{P}_4\text{O}_{48}\text{H}_{32}^{8-}$	Al:559.1 P:415.2 P:425.9 P:415.1 P:413.4	Al:40P:–21 P:–32 P:–21 P:–19
Al3		$\text{Al}_{13}\text{P}_4\text{O}_{52}^{45-}$		$\text{Al}_{13}\text{P}_4\text{O}_{52}\text{H}_{36}^{9-}$	Al:557.3 P:414.0 P:413.5 P:426.8 P:425.9	Al:42P:–20 P:–20 P:–33 P:–32
P4		$\text{Al}_4\text{P}_{12}\text{O}_{44}^{16-}$		$\text{Al}_4\text{P}_{12}\text{O}_{44}\text{H}_{32}^{16+}$	P:415.7Al:563.8Al: 559.4Al:562.3Al:559.6	P:–22Al:35Al: 40Al:37Al:39
P5		$\text{Al}_4\text{P}_{12}\text{O}_{44}^{16-}$		$\text{Al}_4\text{P}_{12}\text{O}_{44}\text{H}_{32}^{16+}$	P:415.3Al:559.3Al: 561.5Al:563.0Al:558.7	P:–21Al:40Al: 37Al:36Al:40

(continued on next page)

Table 2 (continued)

Center atom	Image-before calculation	Formula-before calculation	Image-after calculation	Formula-after calculation	Shielding tensors	Chemical shifts (ppm)
P6		$\text{Al}_4\text{P}_{13}\text{O}_{52}^{27-}$		$\text{Al}_4\text{P}_{13}\text{O}_{52}\text{H}_{36}^{9+}$	P:426.2 Al:559.1 Al:559.1 Al:559.0 Al:559.1	P:–32 Al:40 Al:40 Al:40 Al:40

$\text{AlPO}_4$ -11 with the process described below and calculated their shielding tensors and further chemical shifts. By comparing the calculated chemical shifts with those obtained experimentally, we identified both the possible fragments and the fragments that are unlikely to exist in the crystallization process.

First, we extracted six crystallographically distinct Al- and P-centered large fragments with two completed coordination layers. The shielding tensors of the center atoms were calculated and assigned to the experimentally observed chemical shifts obtained from the highly crystalline  $\text{AlPO}_4$ -11. Because the P and Al atoms nearest to the N atom of the structure-directing agent are P4 and Al1, respectively, the extraction of the fragments is based on P4 and Al1. Finally, we extracted four P4-centered dimers, 12 trimers (Al–P–Al and P–Al–P), eight tetramers (Al–P<sub>4</sub> and P–Al<sub>4</sub>), two pentamers (Al–P<sub>5</sub> and P–Al<sub>5</sub>), and eight types of rings containing P4 and Al1.

### 3.5. Calculation of the chemical shifts of the Al and P atoms in the small fragments and identification of possible small fragments and small fragments unlikely to exist in the crystallization process

In the NMR experiments, the chemical shifts were referenced to a 85%  $\text{H}_3\text{PO}_4$  solution for  $^{31}\text{P}$  and a 1 M  $\text{Al}(\text{NO}_3)_3$  solution for  $^{27}\text{Al}$ . However, both chemicals are not suitable references for the calculation of the chemical shifts of the P and Al atoms in the fragments because the calculation was conducted in a vacuum. A better reference is the framework of  $\text{AlPO}_4$ -11. Considering the limited computing power, we extracted six crystallographically distinct Al- and P-centered large fragments with two completed coordination layers. The shielding tensors of the central Al and P atoms were first calculated. The terminal outer oxygen atoms of these six large fragments were saturated with hydrogen. To ensure that the environment around the central Al and P atoms in the large fragments was identical to that in the framework of  $\text{AlPO}_4$ -11, the structure of the fragments was not optimized. The calculated shielding tensors of the central atoms of these six large fragments were assigned to the experimentally observed chemical shifts to be used as references in the calculations of the chemical shifts of atoms other than Al and P in the small fragments. The experimentally observed chemical shifts of the Al and P atoms in the framework of  $\text{AlPO}_4$ -11 are listed in Table 1. Three resonances centered at –19, –26, and –32 ppm for P and one resonance centered at 37 ppm for Al were observed. In addition, resonances centered at 7 ppm for the aluminum source, at –10 ppm for the six-coordinate Al, at 16 ppm for the five-coordinate Al, at 42 ppm for the four-coordinate Al, at –5 ppm for the P in di-(*i*-propyl)ammonium phosphate, and at –14 ppm for the P in the amorphous aluminophosphate were observed in the crystallization process (Figs. 4 and 5). For

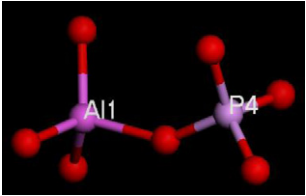
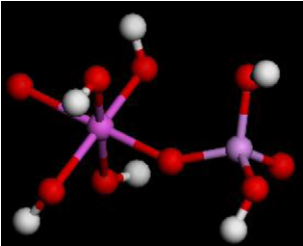
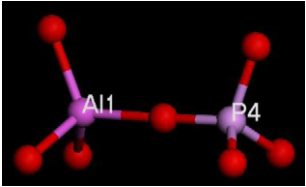
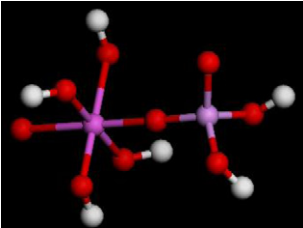
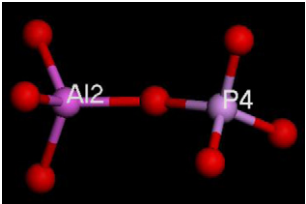
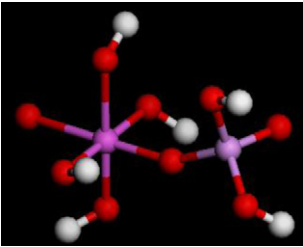

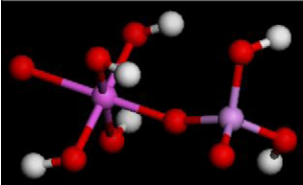
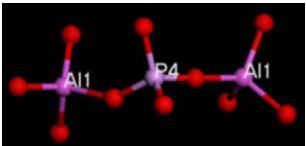
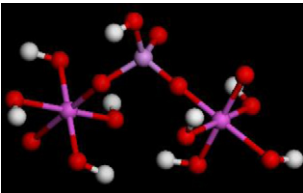
Al, the shielding tensors of 562.7, 559.1, and 557.3 were assigned to the signals at 36, 40, and 42 ppm, respectively. For P, the shielding tensors of 415.7, 415.3, and 426.2 were assigned to the signals at –22, –21, and –32 ppm, respectively. The structure and formula of the six large fragments before and after the calculation and the calculated shielding tensors and related chemical shifts of the central atoms and the atoms of the first coordination layer are listed in Table 2.

Before calculating the shielding tensors of the Al and P atoms in the small fragments, we must estimate the structure of those fragments in the crystallization process. Compared to a P atom, an Al atom has a flexible coordination ability with ligands. For the Al atom connected to one P atom via oxygen, its coordination state could vary from four to six. Therefore, we considered all possibilities for the coordination state of Al (i.e., 4-, 5-, and 6-coordinate) when estimating the structure of dimers. In addition, the protons attached to the oxygen atoms on the P side could also be lost in the crystallization. After considering these situations, we investigated the possible states of Al and P atoms in a dimer. The results indicated that the most likely structure of a dimer is  $(\text{HO})_3\text{HOOAl}-\text{O}-\text{P}(\text{OH})_2\text{O}$  in which the Al atom is coordinated by four  $\text{OH}^-$  ions and one  $\text{O}^{2-}$  ion and the P atom is coordinated by two  $\text{OH}^-$  groups and one O atom. Therefore, we assumed that all Al atoms that are connected to one P atom are coordinated by four  $\text{OH}^-$  ions and one  $\text{O}^{2-}$  ion and that the P atom connected to one, two or three Al atoms via oxygen lost one proton. The bond lengths and angles around the P atom are unchanged. If the Al atom is connected to two or three P atoms, we assume that this Al atom is four-coordinate, and only one of outer oxygen atoms is not saturated with hydrogen. The bond lengths and angles around both Al and P are unchanged. The 34 small fragments were formatted with these rules, and the shielding tensors of the Al and P atoms were calculated. The structures and formulas of these possible fragments before and after the calculation and the calculated shielding tensors and the related chemical shifts are listed in Table 3.

The data in Table 3 show that the calculated chemical shifts for P atoms are within the range of experimentally observed values, whereas those for Al atoms varied significantly. Some of these values for Al atoms are far beyond the observed maximum value. Thus, the calculated chemical shifts for Al atoms are primarily used as a reference in judging whether the small fragments exist in the crystallization process. Because the maximum experimentally observed chemical shift for Al is approximately 40 ppm, we focus mainly on the small fragments that have calculated chemical shifts for Al lower than 40 ppm. In total, 16 of these fragments (four dimers, six trimers in the form of Al–P–Al, four tetramers in the form of P–Al<sub>3</sub>, and two pentamers) are found to have reasonable calculated chemical shifts for both Al and P atoms, which are

**Table 3**

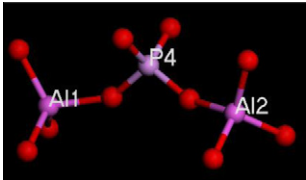
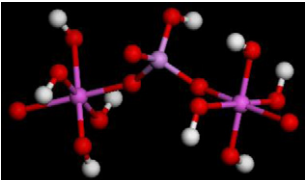
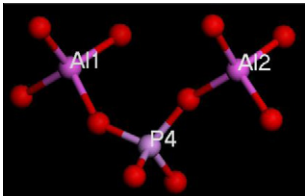
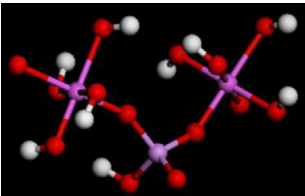
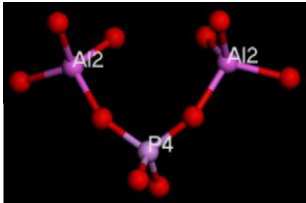
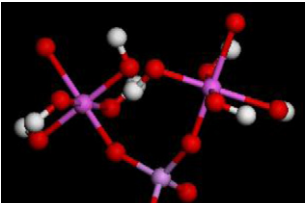
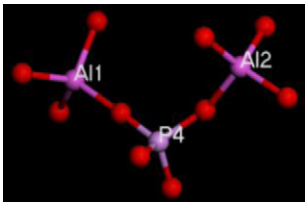
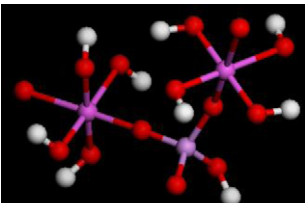
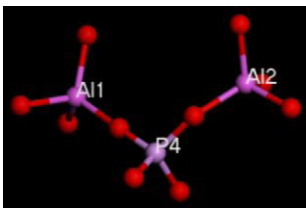
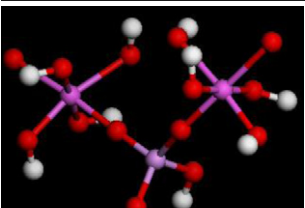
The structures and formulas of the possible fragments before and after the calculation and the calculated shielding tensors and related chemical shifts.

Fragment	Image-before calculation	Formula-before calculation	Image-after calculation	Formula-after calculation	Shielding tensors	Chemical shifts (ppm)
Dimer Al-P		$\text{AlPO}_7^{6-}$		$\text{AlPO}_9\text{H}_6^{4-}$	Al:591.6 P:413.8	Al:8P:–20
		$\text{AlPO}_7^{6-}$		$\text{AlPO}_9\text{H}_6^{4-}$	Al:598.2 P:419.2	Al:1P:–25
		$\text{AlPO}_7^{6-}$		$\text{AlPO}_9\text{H}_6^{4-}$	Al:588.5 P:414.0	Al:5P:–20
		$\text{AlPO}_7^{6-}$		$\text{AlPO}_9\text{H}_6^{4-}$	Al:572.7 P:432.2	Al:27P:–38
Trimer-1 Al-P-Al		$\text{Al}_2\text{PO}_{10}^{9-}$		$\text{Al}_2\text{PO}_{14}\text{H}_9^{8-}$	Al:577.2 Al:577.9 P:418.4	Al:22Al:21P:–16

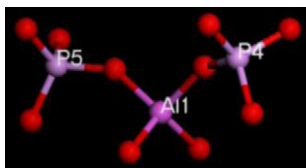
(continued on next page)



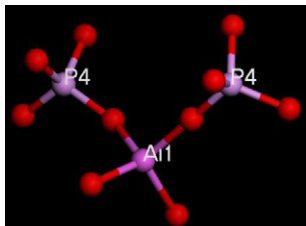
Table 3 (continued)

Fragment	Image-before calculation	Formula-before calculation	Image-after calculation	Formula-after calculation	Shielding tensors	Chemical shifts (ppm)
		$\text{Al}_2\text{PO}_{10}^{9-}$		$\text{Al}_2\text{PO}_{14}\text{H}_9^{8-}$	Al:575.8Al:578.9P:407.4	Al:23Al:20P:–13
		$\text{Al}_2\text{PO}_{10}^{9-}$		$\text{Al}_2\text{PO}_{14}\text{H}_9^{8-}$	Al:573.1Al:578.8P:414.3	Al:26Al:20P:–20
		$\text{Al}_2\text{PO}_{10}^{9-}$		$\text{Al}_2\text{PO}_{14}\text{H}_9^{8-}$	Al:588.6Al:560.9P:437.7	Al:10Al:39P:–44
		$\text{Al}_2\text{PO}_{10}^{9-}$		$\text{Al}_2\text{PO}_{14}\text{H}_9^{8-}$	Al:576.1Al:569.0P:423.1	Al:23Al:30P:–29
		$\text{Al}_2\text{PO}_{10}^{9-}$		$\text{Al}_2\text{PO}_{14}\text{H}_9^{8-}$	Al:573.9Al:575.5P:420.3	Al:25Al:23P:–26

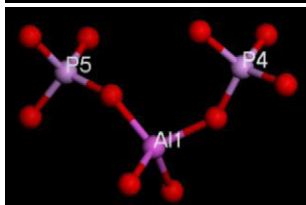
Trimer-2P-Al-  
P



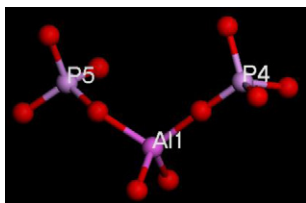
$\text{AlP}_2\text{O}_{10}^{7-}$



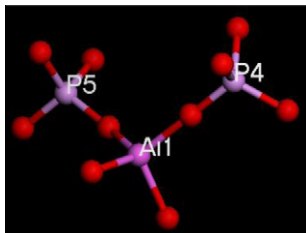
$\text{AlP}_2\text{O}_{10}^{7-}$



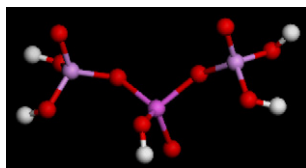
$\text{AlP}_2\text{O}_{10}^{7-}$



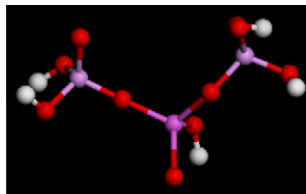
$\text{AlP}_2\text{O}_{10}^{7-}$



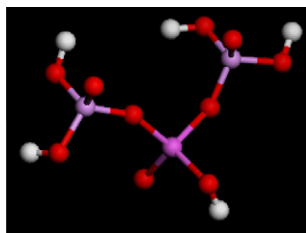
$\text{AlP}_2\text{O}_{10}^{7-}$



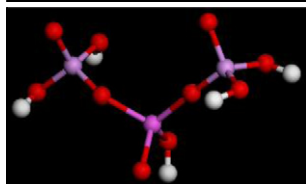
$\text{AlP}_2\text{O}_{10}\text{H}_5^{2-}$



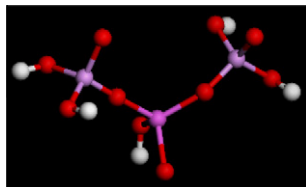
$\text{AlP}_2\text{O}_{10}\text{H}_5^{2-}$



$\text{AlP}_2\text{O}_{10}\text{H}_5^{2-}$



$\text{AlP}_2\text{O}_{10}\text{H}_5^{2-}$



$\text{AlP}_2\text{O}_{10}\text{H}_5^{2-}$

Al:515.9P:397.0P:405.6

Al:78P:P

Al:517.9P:392.0P:404.5

Al:76P:P

Al:519.3P:391.4P:393.4

Al:75P:P:

Al:519.1P:391.4P:399.8

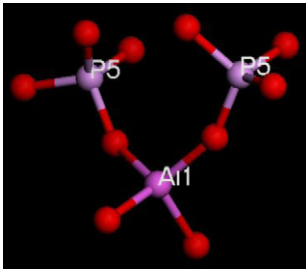
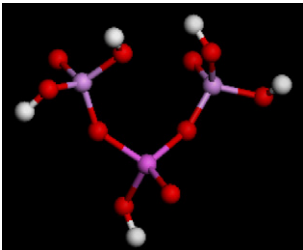
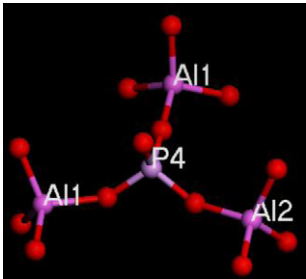
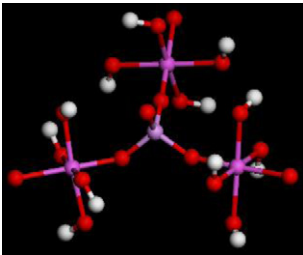
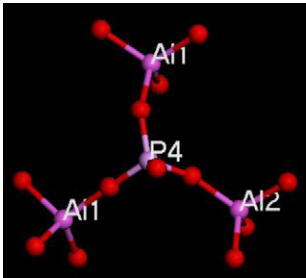
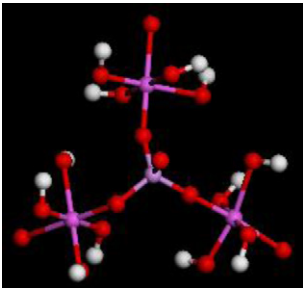
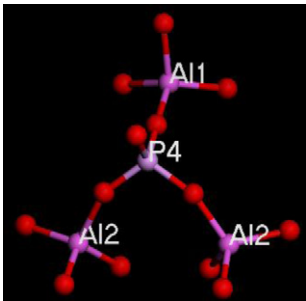
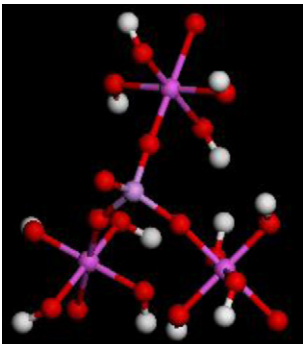
Al:75P:P

Al:520.7P:395.7P:398.5

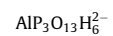
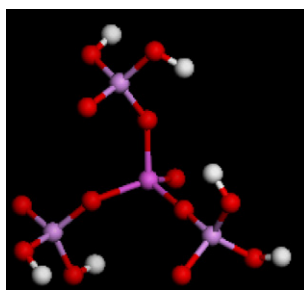
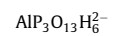
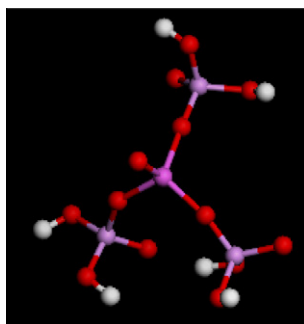
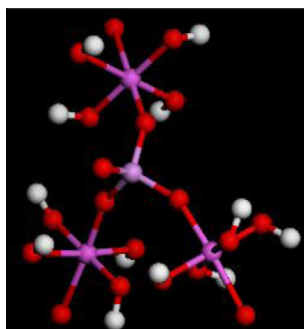
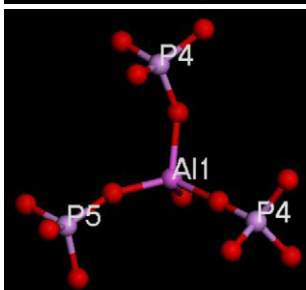
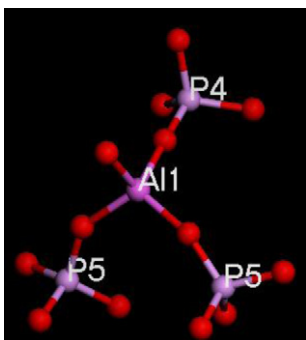
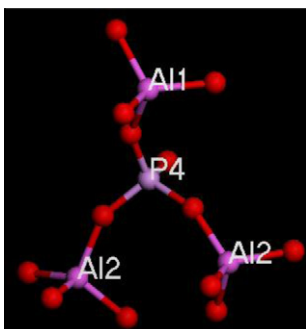
Al:73P:P

(continued on next page)

Table 3 (continued)

Fragment	Image-before calculation	Formula-before calculation	Image-after calculation	Formula-after calculation	Shielding tensors	Chemical shifts (ppm)
Tetramer-1P-Al <sub>3</sub>		AlP <sub>2</sub> O <sub>10</sub> <sup>7-</sup>		AlP <sub>2</sub> O <sub>10</sub> H <sub>5</sub> <sup>2-</sup>	Al:520.3P:394.9P:400.2	Al:74P:P
		Al <sub>3</sub> PO <sub>13</sub> <sup>12-</sup>		Al <sub>3</sub> PO <sub>19</sub> H <sub>12</sub> <sup>12-</sup>	Al:594.0Al:593.5Al:593.4P:416.5	Al:5Al:5Al:5P:–23
		Al <sub>3</sub> PO <sub>13</sub> <sup>12-</sup>		Al <sub>3</sub> PO <sub>19</sub> H <sub>12</sub> <sup>12-</sup>	Al:576.5Al:572.5Al:580.5P:413.3	Al:22Al:26Al:18P:–19
		Al <sub>3</sub> PO <sub>13</sub> <sup>12-</sup>		Al <sub>3</sub> PO <sub>19</sub> H <sub>12</sub> <sup>12-</sup>	Al:581.0Al:576.3Al:574.2P:414.3	Al:18Al:23Al:25P:–20

Tetramer-  
2Al-P<sub>3</sub>



Al:570.4Al:582.0Al:571.5P:412.3

Al:535.6P:393.3P:398.1P:393.2

Al:536.2P:400.0P:391.2P:397.5

Al:29Al:17Al:27P:-18

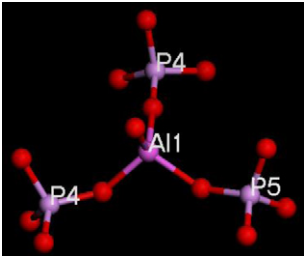
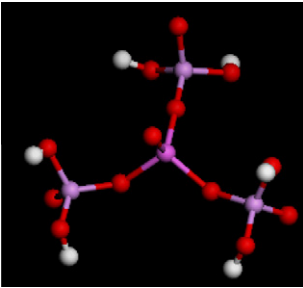
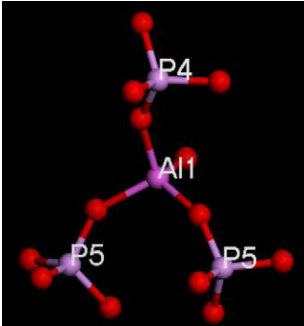
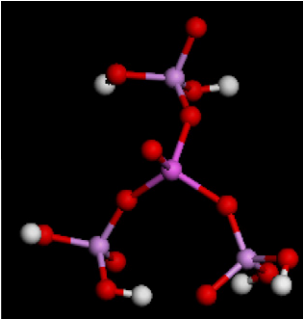
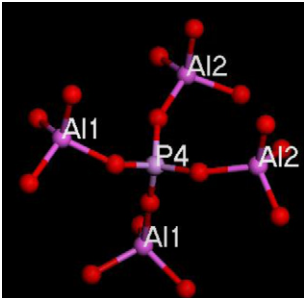
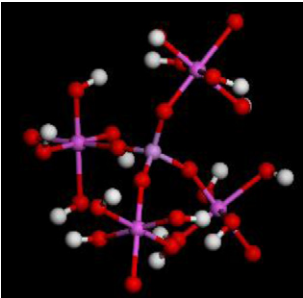
Al:57P:P:P

Al:58P:P:P

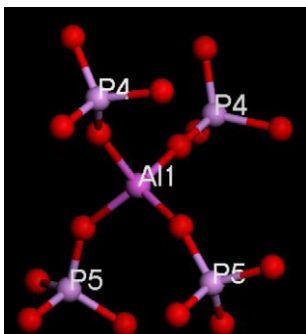
(continued on next page)



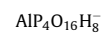
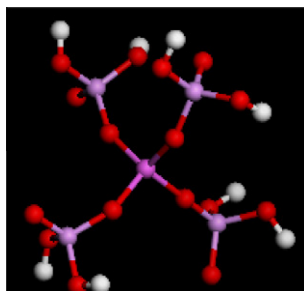
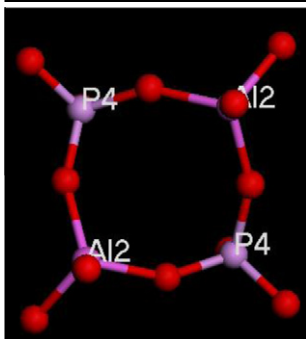
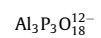
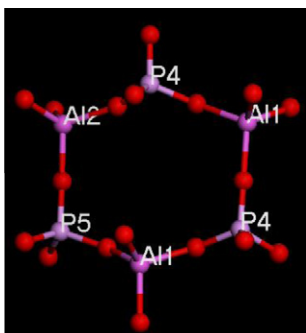
Table 3 (continued)

Fragment	Image-before calculation	Formula-before calculation	Image-after calculation	Formula-after calculation	Shielding tensors	Chemical shifts (ppm)
Pentamer P-Al <sub>4</sub>		$\text{AlP}_3\text{O}_{13}^{8-}$		$\text{AlP}_3\text{O}_{13}\text{H}_6^{2-}$	Al:535.4 P:390.4 P:390.6 P:397.0	Al:59 P:P:P
		$\text{AlP}_3\text{O}_{13}^{8-}$		$\text{AlP}_3\text{O}_{13}\text{H}_6^{2-}$	Al:534.0 P:397.6 P:391.6 P:394.8	Al:61 P:P:P
		$\text{Al}_4\text{PO}_{16}^{15-}$		$\text{Al}_4\text{PO}_{24}\text{H}_{16}^{15-}$	Al:577.4 Al:582.0 Al:575.7 Al:584.2 P:417.0	Al:22 Al:17 Al:23 Al:15 P:–22

PentamerAl-  
P<sub>4</sub>

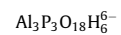
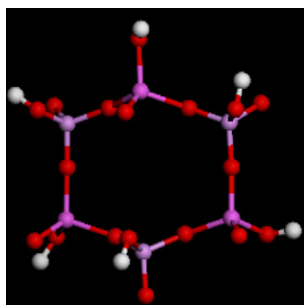


RingP4-starts



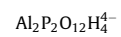
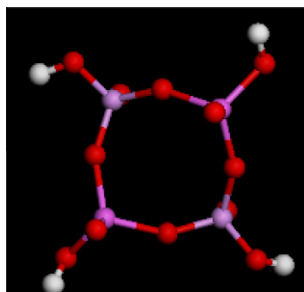
Al:576.8  
P:390.4  
P:403.2  
P:391.0  
P:397.8

Al:39  
P:4P: -9  
P:3P: -4



Al:517.7  
Al:524.5  
Al:521.0  
P:401.9  
P:405.3  
P:408.7

Al:76  
Al:70  
Al:73  
P:P:P



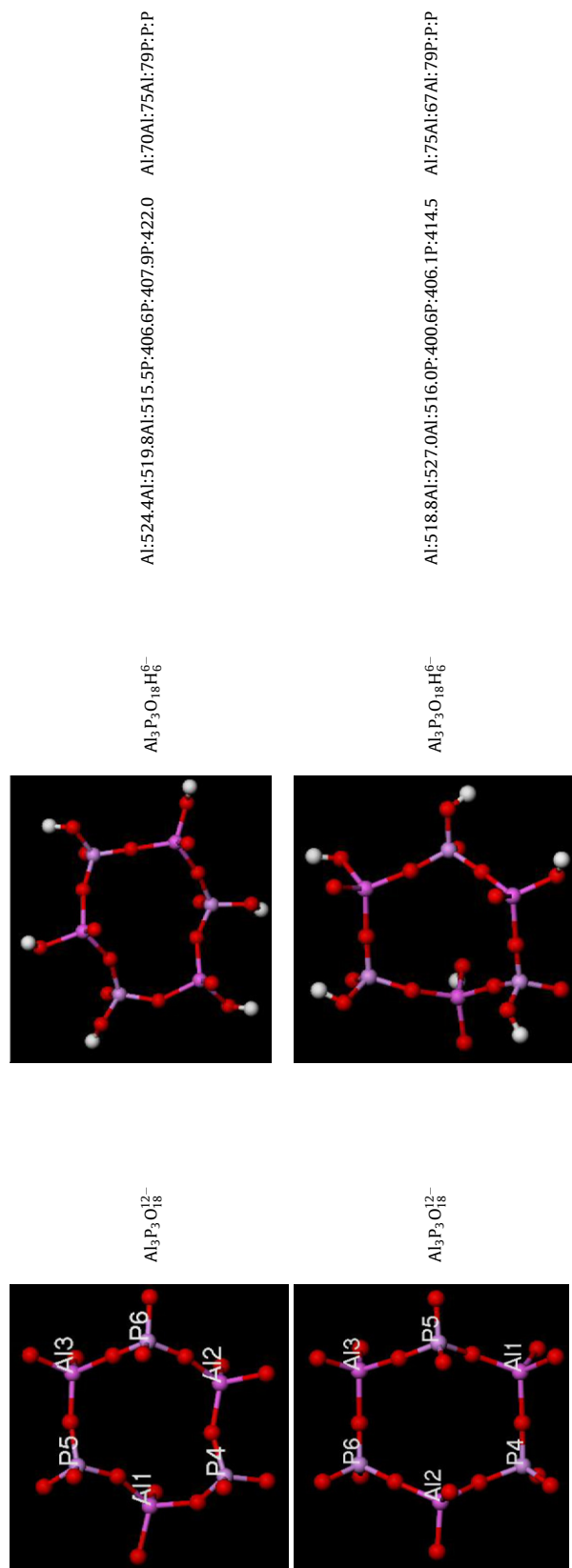
Al:516.1Al:516.P:407.3P:407.7

Al:78  
Al:77  
P:P

(continued on next page)

Table 3 (continued)

Fragment	Image-before calculation	Formula-before calculation	Image-after calculation	Formula-after calculation	Shielding tensors	Chemical shifts (ppm)
RingAl1-starts		$\text{Al}_3\text{P}_3\text{O}_{18}^{12-}$		$\text{Al}_3\text{P}_3\text{O}_{18}\text{H}_6^{6-}$	Al:525.8Al:517.5Al:515.6P:402.5P:407.6P:417.9	Al:68Al:76Al:78P:P:P
		$\text{Al}_3\text{P}_3\text{O}_{18}^{12-}$		$\text{Al}_3\text{P}_3\text{O}_{18}\text{H}_6^{6-}$	Al:522.9Al:522.4Al:516.7P:398.6P:405.9P:406.2	Al:71Al:72Al:77P:P:P
		$\text{Al}_3\text{P}_3\text{O}_{18}^{12-}$		$\text{Al}_3\text{P}_3\text{O}_{18}\text{H}_6^{6-}$	Al:524.3Al:516.1Al:515.3P:406.7P:403.9P:415.4	Al:70Al:78Al:79P:P:P
		$\text{Al}_2\text{P}_2\text{O}_{12}^{8-}$		$\text{Al}_2\text{P}_2\text{O}_{12}\text{H}_4^{4-}$	Al:522.1Al:522.5P:402.8P:401.7	Al:72Al:72P:P



highlighted in bold in Table 3. Therefore, these 16 small fragments may exist in the crystallization process.

In the  $^{31}\text{P}$  MAS NMR spectra of the initial mixture (Fig. 4), in addition to an intense signal centered at  $-5$  ppm, a broad resonance at approximately  $-20$  ppm is observed. The signal centered at  $-5$  ppm can be attributed to phosphate species such as mono-, di-, and poly-phosphates; hydrogen monophosphates; and dihydrogen phosphates, whereas the broad resonance that appeared upfield can be attributed to the amorphous aluminophosphate [67–69]. To identify the fragments in the initial mixture, it is necessary to combine the  $^{27}\text{Al}$  MAS NMR spectra of the initial mixture (Fig. 5) in which a signal from the Al source of Catapal B (7 ppm) and a shoulder resonance from the typical octahedral Al site in aluminophosphate ( $-10$  ppm) were observed. Because the experimentally observed data are from real species, the calculated chemical shifts for a possibly existing fragment must be consistent with the experimental data. After searching the calculated chemical shifts of the extracted small fragments listed in Table 3, we found three dimers and a P-centered tetramer whose calculated chemical shifts for Al atoms are in the range of the experimental data. In the three dimers, the calculated chemical shifts for Al atoms are 8, 1, and 5 ppm, respectively, whereas the three Al atoms in the P-centered tetramer have the same calculated chemical shift of 5 ppm (Table 3). The corresponding calculated chemical shifts for P atoms in these small fragments are all at approximately  $-20$  ppm, which is consistent with the experimentally observed values in the  $^{31}\text{P}$  MAS NMR spectra of the initial mixture. Therefore, these four small fragments possibly existed in the initial mixture. In these four small fragments, the dimer possessing a calculated chemical shift of 1 ppm for Al is the most likely fragment in the initial mixture.

After the initial mixture was heated for 50 min, a significant change in the shape of the  $^{31}\text{P}$  MAS NMR spectrum was observed (Fig. 4). A broad resonance centered at  $-15$  ppm with a shoulder signal at  $-19$  ppm appeared. The obvious resonance centered at  $-15$  ppm can be attributed to the quick increase of the percentage of the amorphous aluminophosphate, whereas the signal at approximately  $-19$  ppm can be attributed to a highly soluble phosphate species because this signal was almost invisible in the  $^{31}\text{P}$  MAS NMR spectrum of the corresponding centrifugation-separated sample from the same autoclave [56]. However, this signal was observed at a low intensity in the  $^{31}\text{P}$  MAS NMR spectrum of the well-crystallized  $\text{AlPO}_4\cdot 11$  [56], suggesting that the environment of P atoms in both cases is very similar. In the corresponding  $^{27}\text{Al}$  MAS NMR spectrum, an intense resonance centered at 42 ppm was observed (Fig. 5). After searching the calculated chemical shifts of the extracted small fragments listed in Table 3, we found an Al-centered pentamer ( $\text{Al}-\text{P}_4$ ) whose calculated chemical shift for Al (39 ppm) is the closest to the experimental data (42 ppm). In addition, the calculated chemical shift for one of the P atoms in this pentamer is approximately  $-9$  ppm, which is consistent with the experimental data. Thus, this fragment possibly existed in the sample heated for 50 min. Because the broad resonance centered at  $-15$  ppm contained many P sites, many other types of fragments must exist in the crystallization process. In fact, many fragments in Table 3 have reasonable calculated chemical shifts for P, including three trimers in the form of  $\text{Al}-\text{P}-\text{Al}$  and three P-centered tetramers ( $\text{P}-\text{Al}_3$ ). However, the corresponding calculated chemical shifts for Al atoms in these fragments are centered at 23 ppm, which is quite far from the experimentally observed value, suggesting that the concentration or percentage of these types of trimers is quite low in the system or that these types of trimers are only the short-lived intermediate of the other type of fragments. The broad resonance observed in this stage may be from the Al-centered pentamers that differ slightly from one another



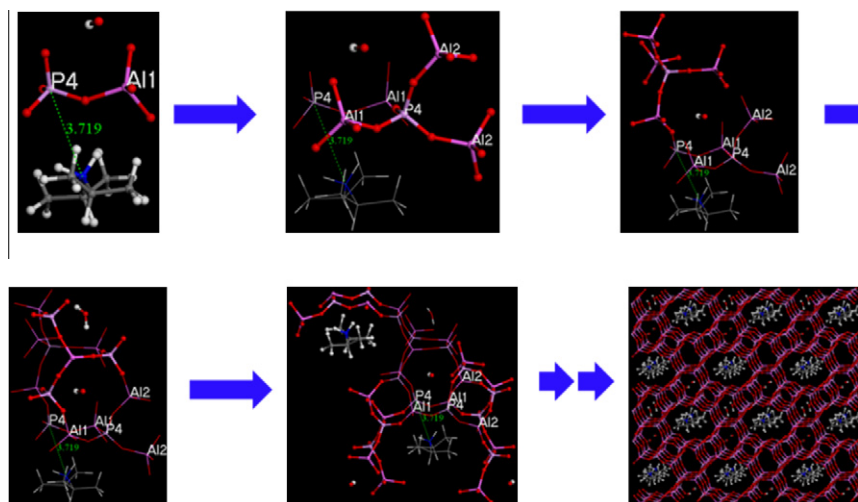


Fig. 7. The proposed crystallization pathway of AlPO<sub>4</sub>-11.

in bond lengths and angles, which resulted in many different but similar P sites.

After prolonging the heating time to 70 min, a new weak resonance centered at 16 ppm was observed in the <sup>27</sup>Al MAS NMR spectrum. The calculated chemical shifts for Al that are closest to this experimentally observed value are from three P-centered tetramers (P–Al<sub>3</sub>) and one P-centered pentamer (P–Al<sub>4</sub>). More than one Al atom is included in these fragments. Some calculated chemical shifts for Al are close to 16 ppm, whereas others are not as close to this number. However, those calculated chemical shifts that differ more from 16 ppm are still within the range of experimentally observed values. The calculated chemical shifts for P atoms in these fragments are all reasonably less than –22 ppm. However, the formation of Al1- and Al2-centered large fragments in this stage is also possible because the calculated chemical shifts for both Al and P atoms are within the range of experimentally observed values (Table 2).

In the <sup>31</sup>P MAS NMR spectrum of the sample heated for 70 min, we found that the intensity of the resonance centered at –19 ppm was significantly enhanced (Fig. 4). This resonance was further enhanced when the heating time was extended to 90 min or 11 h (Fig. 4). Taking into account the fact that this resonance was either embedded in the broad peak or invisible in the <sup>31</sup>P MAS NMR spectra of the samples from the same autoclave but that were separated by centrifugation (Fig. 7 in Ref. [56]), the intense signal centered at –19 ppm can be attributed to a highly soluble phosphate species, as discussed above. The decrease in intensity of the resonances in the upfield region is likely caused by the compression effect of the intense signal centered at –19 ppm.

In the late crystallization stage (90 min and longer), the growth process involving the addition of more fragments to the large composite was almost completed, and the long-range ordering of AlPO<sub>4</sub>-11 was detected by XRD patterns (Fig. 2). The resonances (–32 and –26 ppm) from the well-crystallized AlPO<sub>4</sub>-11 can be observed in the corresponding <sup>31</sup>P MAS NMR spectra (Fig. 4).

On the basis of the possible small fragments being identified by combing the experimental and theoretical data, we can propose a possible crystallization process for AlPO<sub>4</sub>-11 (Fig. 7). In this proposed crystallization process, the protonated structure-directing agent and the dimer fragment moved close to each other in the solution due to an attractive interaction to form a core unit at the beginning of crystallization, which will be included in the final structure of AlPO<sub>4</sub>-11. Along with the crystallization, a P-centered tetramer was added by forming an Al–O–P bond with the Al atom

of the initial dimer. The OH<sup>–</sup> counter ion might be captured at this step. Subsequently, a P-centered pentamer was added to this composite by forming a P–O–Al bond with the P atom of the initial dimer. Along with the crystallization, more monomers, dimers, trimers, tetramers, and pentamers were added to the formed composite to complete the growth of the composite. More structure-directing agents and other guest species (i.e., H<sub>2</sub>O and OH<sup>–</sup>) were captured in this process, which acted as the onset of subsequent crystallization processes. Finally, a periodic three-dimensional structure was formed, which can be described with crystallographic language.

#### 4. Conclusions

The crystallization process of AlPO<sub>4</sub>-11 was investigated. The solid phase throughout the hydrothermal treatment period was freeze-dried, ensuring the complete collection of the small species formed in the crystallization. The solid phase was characterized with XRD and NMR techniques. The quantity and state of the guest species in AlPO<sub>4</sub>-11 was determined by TG, NMR and *in situ* Raman characterization. The location of the guest species was determined with an annealing-based simulation method. A reverse temporal evolution crystallization process was applied to search for the possible fragments formed in the crystallization. Thirty-four possible fragments were extracted from the structure of AlPO<sub>4</sub>-11, and the chemical shift of the Al and P atoms in these fragments were calculated with a quantum mechanics method. By comparing the calculated results with the experimentally observed data, we identified 16 small fragments that may exist in the crystallization process. On the basis of these possibly existing small fragments, a crystallization process for AlPO<sub>4</sub>-11 was proposed. The present study represents a method to identify the possible fragments formed in the crystallization and is a step forward in understanding the crystallization of microporous aluminophosphates at the molecular level.

#### Acknowledgments

We acknowledge the special funding support from the National Natural Science Foundation of China and the National Basic Research Program of China (2011CB808703). W.Y. thanks the Program for New Century Excellent Talents in University (NCET) and the Outstanding Youth Fund of Jilin University for their support.

## References

- [1] R. Xu, W. Pang, J. Yu, Q. Huo, J. Chen, Chemistry of Zeolites and Related Porous Materials: Synthesis and Structure, John Wiley & Sons (Asia) Pte. Ltd., Singapore, 2007.
- [2] P.A. Wright (Ed.), Microporous Framework Solids, The Royal Society of Chemistry, Cambridge, 2008.
- [3] W. Vermeiren, J.P. Gilson, Top. Catal. 52 (2009) 1131–1161.
- [4] A.W. Chester, E.G. Derouane (Eds.), Zeolite Characterization and Catalysis-A Tutorial, Springer, New York, 2009.
- [5] J. Cejka, A. Corma, S.I. Zones (Eds.), Zeolites and Catalysis-Synthesis, Reactions and Applications, WILEY-VCH Verlag GmbH & Co. KGaA, Weinheim, 2010.
- [6] S. Kulprathipanja (Ed.), Zeolites in Industrial Separation and Catalysis, WILEY-VCH Verlag GmbH & Co. KGaA, Weinheim, 2010.
- [7] C. Baerlocher, L.B. McCusker, Database of Zeolite Structures, <http://www.iza-structure.org/databases/>.
- [8] D. Kashchiev, Nucleation: Basic Theory with Applications, Butterworth-Heinemann, Oxford, 2000.
- [9] J.W. Mullin, Crystallization, Butterworth-Heinemann, Oxford, 2001.
- [10] P.G. Vekilov, Cryst. Growth Des. 10 (2010) 5007–5019.
- [11] G.T. Kerr, J. Phys. Chem. 70 (1966) 1047–1050.
- [12] J. Ciric, J. Colloid Interface Sci. 28 (1968) 315–324.
- [13] D.W. Breck, Zeolite Molecular Sieves, Wiley, New York, 1974.
- [14] C.S. Cundy, P.A. Cox, Micropor. Mesopor. Mater. 82 (2005) 1–78.
- [15] S.L. Burkett, M.E. Davis, J. Phys. Chem. 98 (1994) 4647–4653.
- [16] S.L. Burkett, M.E. Davis, Chem. Mater. 7 (1995) 920–928.
- [17] P. de Moor, T.P.M. Beelen, B.U. Komanshek, L.W. Beck, P. Wagner, M.E. Davis, R.A. van Santen, Chem. Eur. J. 5 (1999) 2083–2088.
- [18] R. Ravishanker, C.E.A. Kirschhock, P.P. Knops-Gerrits, E.J.P. Feijen, P.J. Grobet, P. Vanoppen, F.C. De Schryver, G. Miehe, H. Fuess, B.J. Schoeman, P.A. Jacobs, J.A. Martens, J. Phys. Chem. B 103 (1999) 4960–4964.
- [19] C.E.A. Kirschhock, R. Ravishanker, F. Verspeurt, P.J. Grobet, P.A. Jacobs, J.A. Martens, J. Phys. Chem. B 103 (1999) 4965–4971.
- [20] C.E.A. Kirschhock, R. Ravishanker, L. Van Looveren, P.A. Jacobs, J.A. Martens, J. Phys. Chem. B 103 (1999) 4972–4978.
- [21] C.E.A. Kirschhock, R. Ravishanker, P.A. Jacobs, J.A. Martens, J. Phys. Chem. B. 103 (1999) 11021–11027.
- [22] C.E.A. Kirschhock, V. Buschmann, S. Kremer, R. Ravishanker, C.J.Y. Houssin, B.L. Mojet, R.A. van Santen, P.J. Grobet, P.A. Jacobs, J.A. Martens, Angew. Chem. Int. Ed. 40 (2001) 2637–2640.
- [23] C.T.G. Knight, S.D. Kinrade, J. Phys. Chem. B 106 (2002) 3329–3332.
- [24] D.D. Kragten, J.M. Fedeyko, K.R. Sawant, J.D. Rimer, D.G. Vlachos, R.F. Lobo, M. Tsapatsis, J. Phys. Chem. B 107 (2003) 10006–10016.
- [25] H. Ramanan, E. Kokkoli, M. Tsapatsis, Angew. Chem. Int. Ed. 43 (2004) 4558–4561.
- [26] T.M. Davis, T.O. Drews, H. Ramanan, C. He, J.S. Dong, H. Schnablegger, M.A. Katsoulakis, E. Kokkoli, A.V. McCormick, R.L. Penn, M. Tsapatsis, Nat. Mater. 5 (2006) 400–408.
- [27] T.O. Drews, M. Tsapatsis, Micropor. Mesopor. Mater. 101 (2007) 97–107.
- [28] S. Kumar, Z.P. Wang, R.L. Penn, M. Tsapatsis, J. Am. Chem. Soc. 130 (2008) 17284–17286.
- [29] A. Aerts, M. Haouas, T.P. Caremans, L.R.A. Follens, T.S. van Erp, F. Taulelle, J. Vermant, J.A. Martens, C.E.A. Kirschhock, Chem. Eur. J. 16 (2010) 2764–2774.
- [30] A. Aerts, C.E.A. Kirschhock, J.A. Martens, Chem. Soc. Rev. 39 (2010) 4626–4642.
- [31] A. Depla, E. Verheyen, A. Veyfeyken, E. Gobecheva, T. Hartmann, R. Schaefer, J.A. Martens, C.E.A. Kirschhock, Phys. Chem. Chem. Phys. 13 (2011) 13730–13737.
- [32] F.T. Fan, Z.C. Feng, C. Li, Acc. Chem. Res. 43 (2010) 378–387.
- [33] F.T. Fan, Z.C. Feng, C. Li, Chem. Soc. Rev. 39 (2010) 4794–4801.
- [34] C. Kosanovic, K. Havancsak, B. Subotic, V. Svetlicic, T. Misic, A. Cziraki, G. Huhn, Micropor. Mesopor. Mater. 123 (2009) 150–159.
- [35] C. Kosanovic, K. Havancsak, B. Subotic, V. Svetlicic, T.M. Radic, A. Cziraki, G. Huhn, I. Buljan, V. Smrecki, Micropor. Mesopor. Mater. 142 (2011) 139–146.
- [36] S. Kumar, R.L. Penn, M. Tsapatsis, Micropor. Mesopor. Mater. 144 (2011) 74–81.
- [37] L.M. Ren, C.J. Li, F.T. Fan, Q. Guo, D.S. Liang, Z.C. Feng, C. Li, S.G. Li, F.S. Xiao, Chem. Eur. J. 17 (2011) 6162–6169.
- [38] B. Tokay, M. Somer, A. Erdem-Senatalar, F. Schuth, R.W. Thompson, Micropor. Mesopor. Mater. 118 (2009) 143–151.
- [39] W.F. Yan, X.W. Song, R.R. Xu, Micropor. Mesopor. Mater. 123 (2009) 50–62.
- [40] W.F. Yan, L. Xin, V. Olman, J.H. Yu, Y. Wang, Y. Xu, R.R. Xu, Micropor. Mesopor. Mater. 131 (2010) 148–161.
- [41] P. Dauberosguthorpe, V.A. Roberts, D.J. Osguthorpe, J. Wolff, M. Genest, A.T. Hagler, Proteins 4 (1988) 31–47.
- [42] A.D. Becke, J. Chem. Phys. 98 (1993) 5648–5652.
- [43] M.J. Frisch, G.W. Trucks, H.B. Schlegel, G.E. Scuseria, M.A. Robb, J.R. Cheeseman, J.A. Montgomery Jr., T. Vreven, K.N. Kudin, J.C. Burant, J.M. Millam, S.S. Iyengar, J. Tomasi, V. Barone, B. Mennucci, M. Cossi, G. Scalmani, N. Rega, G.A. Petersson, H. Nakatsuji, M. Hada, M. Ehara, K. Toyota, R. Fukuda, J. Hasegawa, M. Ishida, T. Nakajima, Y. Honda, O. Kitao, H. Nakai, M. Klene, X. Li, J.E. Knox, H.P. Hratchian, J.B. Cross, V. Bakken, C. Adamo, J. Jaramillo, R. Gomperts, R.E. Stratmann, O. Yazyev, A.J. Austin, R. Cammi, C. Pomelli, J.W. Ochterski, P.Y. Ayala, K. Morokuma, G.A. Voth, P. Salvador, J.J. Dannenberg, V.G. Zakrzewski, S. Dapprich, A.D. Daniels, M.C. Strain, O. Farkas, D.K. Malick, A.D. Rabuck, K. Raghavachari, J.B. Foresman, J.V. Ortiz, Q. Cui, A.G. Baboul, S. Clifford, J. Cioslowski, B.B. Stefanov, G. Liu, A. Liashenko, P. Piskorz, I. Komaromi, R.L. Martin, D.J. Fox, T. Keith, M.A. Al-Laham, C.Y. Peng, A. Nanayakkara, M. Challacombe, P.M.W. Gill, B. Johnson, W. Chen, M.W. Wong, C. Gonzalez, J.A. Pople, Gaussian 03, Revision B.03, Gaussian Inc., Pittsburgh, PA, 2003.
- [44] J.M. Bennett, J.W. Richardson, J.J. Pluth, J.V. Smith, Zeolites 7 (1987) 160–162.
- [45] Materials Studio V4.0, Accelrys Software Inc., San Diego, 2005.
- [46] R.G. Parr, W. Yang, Density-Functional Theory of Atoms and Molecules, Oxford University Press, New York, 1989.
- [47] K. Wolinski, J.F. Hinton, P. Pulay, J. Am. Chem. Soc. 112 (1990) 8251–8260.
- [48] S.T. Wilson, B.M. Lok, C.A. Messina, T.R. Cannan, E.M. Flanigen, J. Am. Chem. Soc. 104 (1982) 1146–1147.
- [49] S.T. Wilson, B.M. Lok, E.M. Flanigen, US Patent 4310,440 (1982).
- [50] J.H. Yu, R.R. Xu, Acc. Chem. Res. 36 (2003) 481–490.
- [51] J.H. Yu, R.R. Xu, Chem. Soc. Rev. 35 (2006) 593–604.
- [52] Y. Li, J.H. Yu, R.R. Xu, ALPO Database <<http://mezeopor.jlu.edu.cn/alpo/>>.
- [53] W.F. Yan, J.H. Yu, R.R. Xu, G.S. Zhu, F.S. Xiao, Y. Han, K. Sugiyama, O. Terasaki, Chem. Mater. 12 (2000) 2517–2519.
- [54] Y.N. Huang, R. Richer, C.W. Kirby, J. Phys. Chem. B 107 (2003) 1326–1337.
- [55] B. Chen, Y. Huang, J. Phys. Chem. C 111 (2007) 15236–15243.
- [56] B. Zhang, J. Xu, F.T. Fan, Q. Guo, X. Tong, W.F. Yan, J.H. Yu, F. Deng, C. Li, R.R. Xu, Micropor. Mesopor. Mater. 147 (2012) 212–221.
- [57] N.J. Tapp, N.B. Milestone, D.M. Bibby, Zeolites 8 (1988) 183–188.
- [58] S.M. Golubev, Y.D. Kondrashev, J. Struct. Chem. 25 (1984) 471–473.
- [59] M.T. Averbuchpouchot, A. Durif, Acta Crystallogr., Sect. C: Cryst. Struct. Commun. 43 (1987) 1894–1896.
- [60] S. Kamoun, A. Jouini, A. Daoud, Acta Crystallogr., Sect. C: Cryst. Struct. Commun. 47 (1991) 117–119.
- [61] S. Kamoun, A. Jouini, A. Daoud, A. Durif, J.C. Guitel, Acta Crystallogr., Sect. C: Cryst. Struct. Commun. 48 (1992) 133–135.
- [62] D. Riou, T. Loiseau, G. Ferey, Acta Crystallogr., Sect. C: Cryst. Struct. Commun. 49 (1993) 1237–1238.
- [63] S.R.J. Oliver, A.J. Lough, G.A. Ozin, Inorg. Chem. 37 (1998) 5021–5028.
- [64] B. Han, C.H. Shin, P.A. Cox, S.B. Hong, J. Phys. Chem. B 110 (2006) 8188–8193.
- [65] N. Dufau, L. Luciani, F. Rouquerol, P. Llewellyn, J. Mater. Chem. 11 (2001) 1300–1304.
- [66] J.G. Longstaffe, B.H. Chen, Y.N. Huang, Micropor. Mesopor. Mater. 98 (2007) 21–28.
- [67] A.R. Grimmer, U. Haubenreisser, Chem. Phys. Lett. 99 (1983) 487–490.
- [68] I.L. Mudrakovskii, V.P. Shmachkova, N.S. Kotsarenko, V.M. Mastikhin, J. Phys. Chem. Solids 47 (1986) 335–339.
- [69] P. Hartmann, J. Vogel, B. Schnabel, J. Magn. Reson., Ser. A 111 (1994) 110–114.